

# Determination of the Initiation and Propagation Mechanism of Fireside Corrosion

B. S. Lutz<sup>1</sup> · G. R. Holcomb<sup>2</sup> · G. H. Meier<sup>1</sup>

Received: 18 March 2015 / Revised: 9 June 2015 / Published online: 23 June 2015  
© Springer Science+Business Media New York 2015

**Abstract** A variety of deposit compositions were examined in short-term laboratory tests with the aim of determining the corrosion mechanisms of fireside corrosion for a range of chromia-forming alloys in various combustion systems. The deposits formed in boilers are complex, and despite decades of study, the propagation mechanism of fireside corrosion is not well understood. Alkali iron trisulfates, which are stabilized by  $\text{SO}_3$  in the gas atmosphere, have been cited to be the major corrosive species for many years. The propagation mechanism for fireside corrosion was investigated using T92 (a typical ferritic boiler steel) and a model austenitic Fe–Ni–Cr alloy in contact with synthetic coal ash deposits. The metal loss, corrosion product morphologies, and compositions were carefully characterized to define a propagation mechanism. The corrosive species responsible for degradation was a  $(\text{Na,K})_2\text{SO}_4\text{--Fe}_2(\text{SO}_4)_3$  solution and not alkali iron trisulfates. The formation of the liquid deposit is similar to Type II hot corrosion of components in gas turbine engines. The mechanism is a synergistic dissolution process, where simultaneous basic and acidic dissolution of protective  $\text{Cr}_2\text{O}_3$  and  $\text{Fe}_2\text{O}_3$  disrupts protective oxide formation and locally produces negative solubility gradients at the oxide/salt interface. The dissolved  $\text{Fe}_2\text{O}_3$  and  $\text{Cr}_2\text{O}_3$  precipitate where there is lower solubility, creating the observed corrosion products. The effect of the deposit composition was examined with respect to the proposed fireside corrosion mechanism. These measurements were found to be consistent with the proposed mechanism based on synergistic fluxing.

**Keywords** Fireside corrosion · Hot corrosion · Coal-fired boilers

---

✉ G. H. Meier  
ghmeier@pitt.edu

<sup>1</sup> Mechanical Engineering and Materials Science Department, University of Pittsburgh, Benedum Engineering Hall, Pittsburgh, PA 15261, USA

<sup>2</sup> National Energy Technology Laboratory, 1450 Queen Avenue SW, Albany, OR 97321, USA

## Introduction

Fireside corrosion occurs in the heat exchanger components of coal-fired power plants by gas phase oxidation along with molten deposits, which produce liquid-phase corrosion. Fireside corrosion can result in general mass loss or the formation of cracks which then allow failure by mechanical mechanisms such as fatigue [1]. Chromium has been shown to be the most beneficial alloying element for corrosion resistance [2]. The temperature range of interest, the gas atmosphere, and the deposits will determine the type of corrosion which will occur. In the United States, the coals are characterized based on their inorganic constituents as “Eastern” or “Western” coals. Western coals are typically described as those for which the  $\text{CaO} + \text{MgO}$  content exceeds the  $\text{Fe}_2\text{O}_3$  content of the ash, while the reverse is true for Eastern coals. The inorganic materials in Eastern coals are bituminous and are predominantly in the form of discrete mineral particles. Clay minerals such as kaolin or illite, as well as quartz and pyrite, are dominant. Western coals are usually lignites or subbituminous [3]. Tables 1 and 2 list the typical compositions of an Eastern and Western United States coal ash [3]. Oxy-fuel combustion produces flue gases containing approximately 60 %  $\text{CO}_2$ –30 %  $\text{H}_2\text{O}$ –4 %  $\text{O}_2$ –5 %  $\text{N}_2$ , whereas traditional air-fired combustion produces flue gases containing approximately 74 %  $\text{N}_2$ –12 %  $\text{CO}_2$ –9 %  $\text{H}_2\text{O}$ –4 %  $\text{O}_2$  [2].  $\text{SO}_2$  in the flue gas and ash deposits from the fuel cause severe corrosion in the superheater and reheater tubes of coal fired boilers where the tube temperatures are the highest. In the temperature range of interest (650–750 °C), alkali iron trisulfates have been considered the main contributor to fireside corrosion [4]. This is due to the fact that they have melting points below the temperature range of interest, they are highly reactive, and they have been found in areas of corrosion [4]. Whether or not the alkali iron trisulfates are the corrosive species needs to be determined. It is also possible accelerated corrosion is the result of a low melting  $(\text{Na,K})_2\text{SO}_4$ – $\text{Fe}_2(\text{SO}_4)_3$  eutectic which forms by the reaction of a

**Table 1** Mineral distribution of typical eastern and western U.S. coals [3]

Eastern coals			Western coals		
Mineral distribution			Mineral distribution		
Mineral	Range	Typical	Mineral	Range	Typical
Quartz	5–44	18	Quartz	7–22	15
Kaolinite	9–60	32	Kaolinite	13–45	30
Illite	2–29	14	Illite	0–12	2
Chlorite	0–15	2	Mixed silicates	0–22	8
Mixed silicates	5–31	17	Pyrite	1–26	7
Pyrite	1–27	8	Fe-sulfates	0–5	1
Calcite	0–14	3	Fe-rich	0–14	2
Siderite/ankerite	0–11	2	Ca-rich	7–49	25
Other minerals	0–12	4	Other minerals	1–10	7

**Table 2** Ash composition of typical eastern and western U.S. coals [3]

Eastern coals		Western coals	
Typical ash chemistry		Typical ash chemistry	
Species	wt%	Species	wt%
SiO <sub>2</sub>	54	SiO <sub>2</sub>	30
Al <sub>2</sub> O <sub>3</sub>	29	Al <sub>2</sub> O <sub>3</sub>	15
Fe <sub>2</sub> O <sub>3</sub>	8	Fe <sub>2</sub> O <sub>3</sub>	10
CaO	2	CaO	20
MgO	1	MgO	8
K <sub>2</sub> O	1	K <sub>2</sub> O	0.7
Na <sub>2</sub> O	1	Na <sub>2</sub> O	0.6
TiO <sub>2</sub>	1	TiO <sub>2</sub>	0.7
P <sub>2</sub> O <sub>5</sub>	0.2	P <sub>2</sub> O <sub>5</sub>	0.4
SO <sub>3</sub>	2	SO <sub>3</sub>	15

thermally grown iron oxide scale on the surface of the heat exchanger components or iron oxides from the ash with SO<sub>3</sub> (oxidized from SO<sub>2</sub>) in the gas atmosphere due to sulfur in the coal and alkali sulfates in the coal ash that deposit on the surface. The amount of corrosion increases with increasing concentrations of SO<sub>2</sub> and alkali sulfates. The temperature, which corresponds to the maximum metal loss, follows a bell-shaped curve with a maximum between 650 and 750 °C. The curve may be shifted based on alloy composition, SO<sub>2</sub> level and alkali content [5–7].

The deposits formed in boilers are complex, and despite decades of study, the propagation mechanism of fireside corrosion is not well understood. Because SO<sub>3</sub> enters the deposit from the gas phase, the solubility gradient for the oxides of the underlying metal alloying elements should be positive, which should eliminate self-sustaining fluxing and degradation. However, fireside corrosion is known to be a self-sustaining form of attack. Currently ferritic/martensitic stainless steels or austenitic stainless steels are used as boiler tube materials. The propagation mechanism for fireside corrosion was therefore investigated using T92 (a typical ferritic/martensitic boiler steel) and a model Fe–Ni–Cr alloy and synthetic coal ash deposits. The kinetics and corrosion product morphologies and compositions were carefully characterized to define a propagation mechanism.

## Experimental Procedures

Two different alloys were used in this mechanism study. T92 is a commercial ferritic boiler steel used in coal-fired power plants. It has about 9 % Cr, which should not be enough to form a Cr<sub>2</sub>O<sub>3</sub> scale and will therefore form a Fe–Cr spinel scale when oxidized in the absence of a deposit [8]. A model austenitic alloy was prepared with 12 % Ni and 18 % Cr. Austenitic stainless steel will provide greater protection with the higher chromium contents, and this alloy has a composition similar to type 347 stainless steels used in coal-fired power plants in high

temperature applications. The compositions of the alloys are presented in Table 3. The alloys were cut into rectangular coupon specimens approximately 14–16 mm × 8–13 mm × 2–4 mm. All of the specimens were polished to a 1200P grit SiC finish and ultrasonically cleaned in isopropanol. The specimens were then dried and weighed before any deposits were applied. Two deposits were used in the testing of these alloys. These deposits include:

1.  $\text{Na}_2\text{SO}_4:\text{K}_2\text{SO}_4$  in a 1:1 molar ratio (designated as M1). This deposit will remain solid until it reacts with sufficient thermally grown iron oxide and  $\text{SO}_3$  in the gas atmosphere to form a liquid  $(\text{Na,K})_2\text{SO}_4\text{--Fe}_2(\text{SO}_4)_3$  solution. This allows for analysis of the fireside corrosion propagation mechanism and the importance of a thermally grown iron oxide scale in liquid formation.
2.  $\text{Na}_2\text{SO}_4:\text{K}_2\text{SO}_4:\text{Fe}_2\text{O}_3$  in a 1.5:1.5:1.0 molar ratio. This is the so-called standard corrosion mix (SCM). The ratios for this mix are the stoichiometric coefficients of alkali iron trisulfates. This deposit is designed to form alkali iron trisulfates even without the presence of thermally grown iron oxides on the specimen surface.

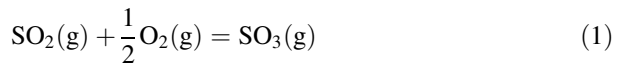
The specimens were placed into alumina crucibles so that half of the specimen was covered by powder and half was not so the effect of deposit thickness on the corrosion of the alloy could be determined. This provides three deposit zones for each specimen: a thick deposit zone (where the specimen is buried in the deposit), a thin deposit zone (where the deposit powder first covers the specimen), and a no-deposit zone.

## Test Procedure

The crucibles were placed into a silica tube in a horizontal resistance-heated furnace. The specimens were cycled into and out of the hot zone of the furnace manually using a magnet to push a silica rod, which held the specimen holder, consisting of two crucibles hung by Kanthal wire below the silica rod. The specimens could be cycled in and out of the furnace so that they reach the test temperature in approximately 1 min. The hot zone was maintained within 3 °C of the test temperature. The gas atmosphere tested contains oxygen with 1000 ppm  $\text{SO}_2$ . The gas flowed into the tube at a constant flow rate of 15 mL/min (0.0125 cm/s) and passed over a platinum honeycomb catalyst placed in the hot zone of the furnace to establish the equilibrium  $p_{\text{SO}_3}$ , described by Eq. 1.

**Table 3** Composition of alloys tested (wt%)

	Fe	Ni	Cr	Mo
T92	Balance	0.32	9	0.32
FeNiCr	Balance	12	18	–



The equilibrium  $p_{\text{SO}_3}$  value at 700 °C for the tested gas atmosphere was calculated to be  $7.16 \times 10^{-4}$  atm. The equilibrium established in Eq. 1 was used along with HSC Chemistry software to determine the  $\text{SO}_3$  partial pressure. It was validated by hand calculation, using the concentration of the gas and Gibbs free energy values. When exiting the furnace, the gas was bubbled through an aqueous  $\text{Na}_2\text{CO}_3$  solution to remove  $\text{SO}_3$  before entering the fume hood.

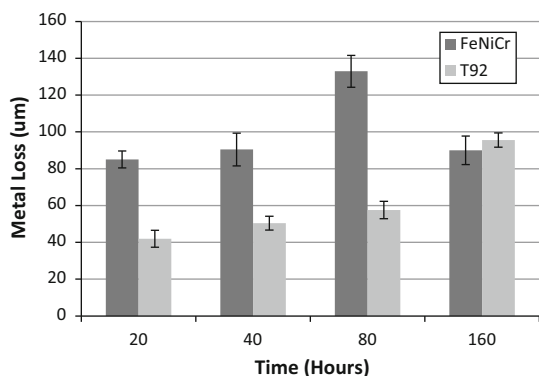
The alloys in Table 1 were exposed at 700 °C with both deposits described in the previous section for durations of 20, 40, 80, and 160 h. This allowed for the examination of the initiation and propagation mechanisms. The specimens were metallographically prepared for examination with oil instead of water to preserve water soluble corrosion products.

## Evaluation of Specimens

The extent of attack on the specimens was analyzed from weight change measurements and metal loss calculations. Metal loss calculations provide the most reliable measurement of the corrosion damage to alloys, as they are unaffected by deposit material adhering to the specimen [9]. The results were plotted as metal loss values according to the draft standards for high temperature corrosion measurements [10]. This was done by measuring the thickness of intact metal remaining in cross-sectional images and subtracting from the initial metal thickness and then dividing by 2 to obtain the metal loss of one surface. The thickness and compositions of the corrosion products along with the metal loss calculations give a better understanding of the amount and type of degradation that occurred.

Macroscopic images of the specimens were taken after each test. X-ray diffraction was used to characterize the corrosion products. The surfaces and cross-sections were viewed under a scanning electron microscope: a JEOL JSM-6610LV SEM microscope equipped with secondary electron (SE), backscatter electron

**Fig. 1** Thick deposit zone metal loss of FeNiCr and T92 exposed at 700 °C with the M1 deposit in  $\text{O}_2 + 1000$  ppm  $\text{SO}_2$



(BSE), and X-ray detectors for performing energy dispersive spectroscopic analysis (EDS). The accelerating voltage used was 20 kV.

## Results

### M1 Results

The M1 deposit should remain solid on the surface of the test specimens until it reacts with a thermally grown iron oxide scale and sufficient  $\text{SO}_3$  from the gas atmosphere. The extent of the corrosion can be seen in the plot of metal loss in the thick deposit zone of both alloys in Fig. 1. The error bars are the standard error for at least 20 metal loss measurements for each specimen.

Both of the alloys were severely degraded using the M1 deposit. Chromium is believed to be the best alloying element for corrosion resistance, however the model austenitic alloy had more weight gain and metal loss than T92 at most durations, even though it has twice the amount of chromium. Significant metal losses occur in a short amount of time as the alloys are in the propagation stage after 20 h, at which point the amount of degradation is independent of the alloy composition. The metal losses are consistent with the macroscopic and microscopic images in Figs. 2, 3, 4, 5, 6 and 7.

Cross-sectional SEM images of the results for T92 in the three different deposit zones are presented in Figs. 2, 3 and 4. The images which are presented are typical of the extent of corrosion and the corrosion products and morphologies for each deposit zone. In the no-deposit zone and in areas which were not yet degraded, chromium and iron rich spinel oxide scales grew with alkali sulfate rich deposit still on top. As time increases (80–160 h) the corrosion spreads into the no-deposit zone, and the protective Fe–Cr spinel scale has broken down. The corrosion products consist of thicker external  $\text{Fe}_2\text{O}_3$  scales over top of internal iron and chromium rich spinel oxide with sulfides at the base of the corrosion pits. The thicker, non-

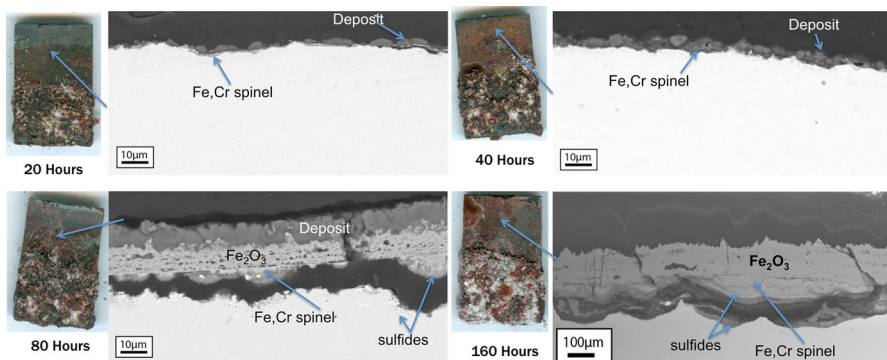


**Fig. 2** Cross-sectional micrographs of the non-deposit zone of T92 tested at 700 °C with the M1 deposit in a crucible in  $\text{O}_2 + 1000 \text{ ppm SO}_2$  for 20, 40, 80, and 160 h

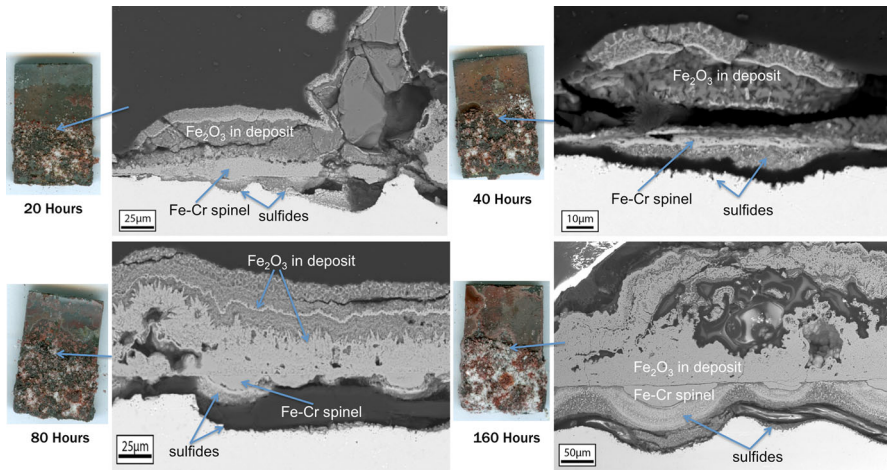


**Fig. 3** Cross-sectional micrographs of the thin-deposit zone of T92 tested at 700 °C with the M1 deposit in a crucible in  $O_2 + 1000 \text{ ppm } SO_2$  for 20, 40, 80, and 160 hours

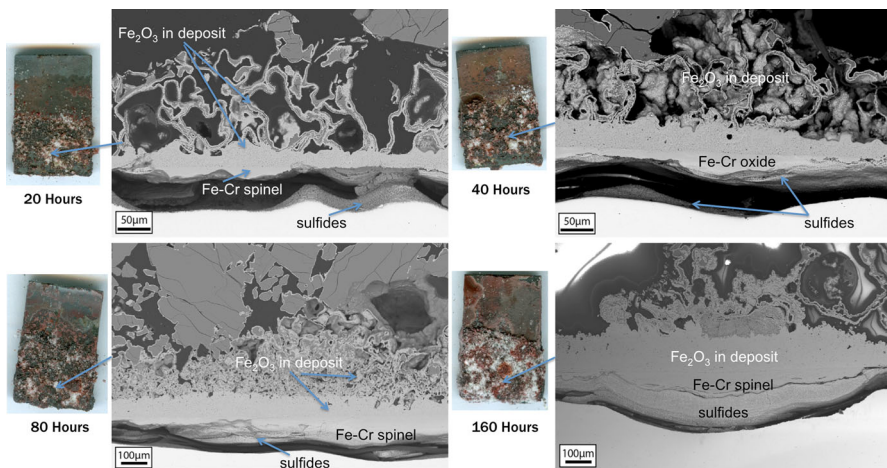


**Fig. 4** Cross-sectional micrographs of the thick-deposit zone of T92 tested at 700 °C with the M1 deposit in a crucible in  $O_2 + 1000 \text{ ppm } SO_2$  for 20, 40, 80, and 160 h

protective iron oxide scales are expected with FeCr–FeCrNi alloys after breakdown of the protective Cr rich scale [11, 12]. This can be explained by the different diffusivities of Fe and Cr in spinel [13]. The liquid migrated up the specimens and this migration was a precursor to the corrosion spreading. The thick and thin deposit zones were severely degraded after each test duration. The corrosion started out covering large areas in the deposit zone, and these areas and the amount of corrosion increased with time until the entire deposit zone was completely degraded. The corrosion products consisted of external thick porous  $Fe_2O_3$  scales which grew

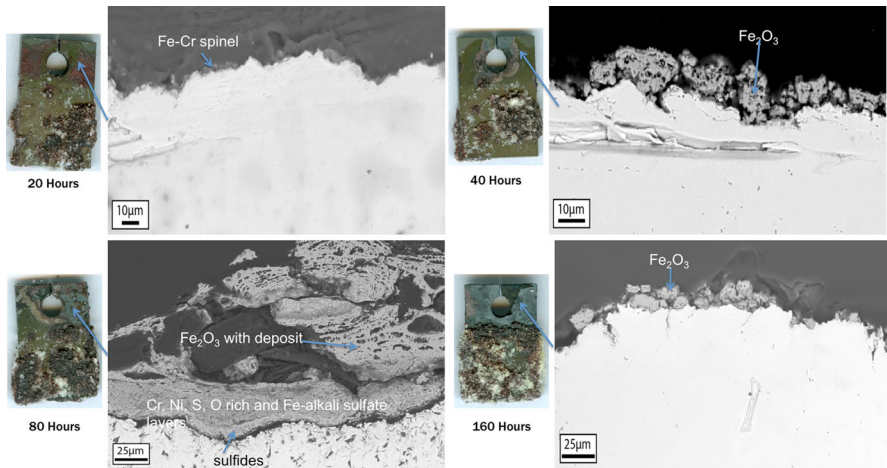


**Fig. 5** Cross-sectional micrographs of the no deposit zone of FeNiCr tested at 700 °C with the M1 deposit in a crucible in  $O_2 + 1000 \text{ ppm } SO_2$  for 20, 40, 80, and 160 h

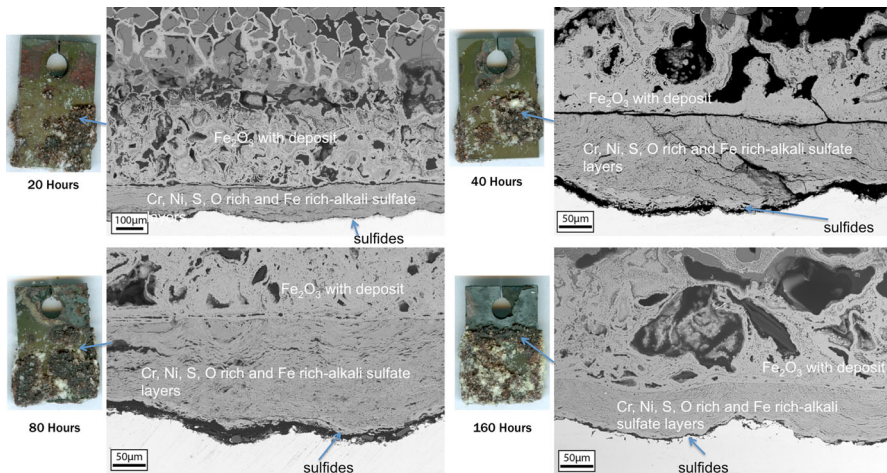


**Fig. 6** Cross-sectional micrographs of the thin deposit zone of FeNiCr tested at 700 °C with the M1 deposit in a crucible in  $O_2 + 1000 \text{ ppm } SO_2$  for 20, 40, 80, and 160 h

around remaining alkali sulfates from the deposit. Below the thick iron oxide scales are internal corrosion pits rich in Cr, Fe, S, and O. The sulfur content increases with depth into the pits until a thick layer of iron and chromium sulfide (identified with EDS) forms at the base.

Cross-sectional SEM images for the results in the three deposit zones of FeNiCr at each test duration are presented in Figs. 5, 6 and 7. Again, these images are typical of the corrosion products and morphologies of each deposit zone. In the no-deposit zone, a thin iron chromium rich spinel oxide scale grew after 20 h, but as



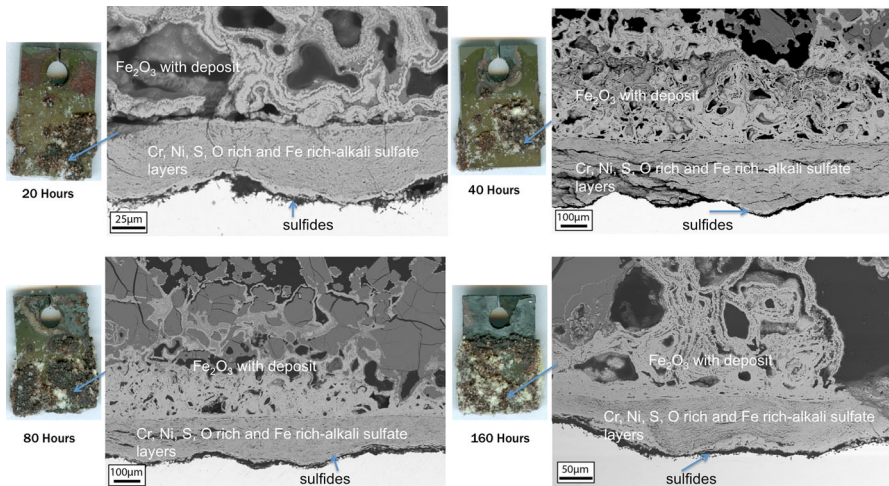
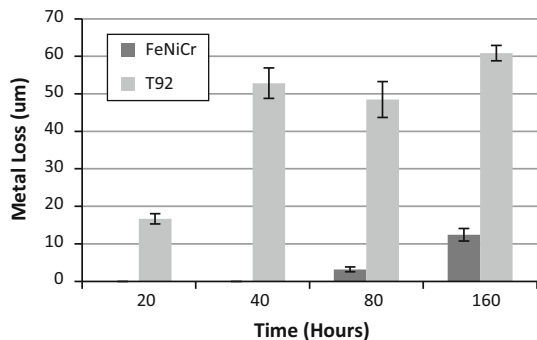


**Fig. 7** Cross-sectional micrographs of the thick deposit zone of FeNiCr tested at 700 °C with the M1 deposit in a crucible in O<sub>2</sub> + 1000 ppm SO<sub>2</sub> for 20, 40, 80, and 160 h

time increased, the protective scales broke down and developed into thicker Fe<sub>2</sub>O<sub>3</sub> and eventually the corrosion spread from the deposit zone up into the no-deposit zone where thick, porous external Fe<sub>2</sub>O<sub>3</sub> scales grew over top of internal pits after 80 h. The results are similar to those for T92 for the thick and thin deposit zones, even though the chromium content is double for the FeNiCr alloy. Areas of corrosion can be seen after 20 and 40 h. They are not as large as those on T92, so the higher chromium content may offer a little protection, but these areas quickly spread with time until the entire deposit zone was degraded. The corrosion products were similar to T92, but the chromium sulfide layer at the base of the corrosion pits was not as extensive, and some nickel was detected in regions of the internal scale. The corrosion pits formed a layered structure with a layer rich in Cr, S, and O and a layer rich in Fe and alkali sulfates. This layered structure corresponds with the proposed corrosion mechanism, which will be described in a subsequent section.

**Fig. 8** Thick deposit zone metal loss of FeNiCr and T92 oxidized at 700 °C in O<sub>2</sub> + 1000 ppm SO<sub>2</sub> with the standard corrosion mix powder in a crucible



## SCM Results

The deposit was designed to form alkali iron trisulfates even without the presence of thermally grown iron oxides on the specimen surface. The extent of the corrosion can be seen in the metal loss plot in thick deposit zones shown in Fig. 8. The metal loss plot shows significant metal loss for T92 even after 20 h. FeNiCr exhibits an initiation stage, and propagation of corrosion does not take place until after 80 h of exposure. After 160 h, the metal loss was still much less than for T92. The lack of initiation stage in T92 and the fact that the FeNiCr alloy has an initiation stage may be due to the difference in chromium content in the alloys. More chromium in the alloy may be delaying the onset of corrosion by continuously forming a protective chromium oxide layer on the surface and temporarily preventing any liquid melt that has formed from transient iron oxides or from iron oxides in the deposit from producing corrosion. This is the initiation stage. Eventually the  $\text{Cr}_2\text{O}_3$  scale breaks down or is dissolved, and there are insufficient amounts of Cr to maintain it and non-protective  $\text{Fe}_2\text{O}_3$  scales form allowing for the liquid melt to reach the metal surface. This is when the propagation stage begins.

Cross-sectional SEM images for each deposit zone for T92 at each of the test durations are shown in Figs. 9, 10 and 11. In the non-deposit zone, thin iron and chromium rich spinel oxide scales grew on the surface. A thicker  $\text{Fe}_2\text{O}_3$  scale grew after 160 h. The liquid has migrated up the specimens and encroached into the no-deposit zone as was mentioned previously with the M1 deposit. This would result in corrosion if the test was run for a longer duration. Severe corrosion occurred throughout the entire deposit zone during each duration. The cross-sectional images match well with the lack of initiation stage and the amount of rapid metal loss shown in the metal loss plot. The corrosion products are similar to those for the M1 deposit. Thick, porous, external  $\text{Fe}_2\text{O}_3$  scales grew and surrounded remaining alkali sulfates in the deposit. These grew over internal pits rich in Cr, Fe, S, and O with a thick sulfide layer at the base. The pits grew with time until they coalesced to form a continuous corrosion product layer.

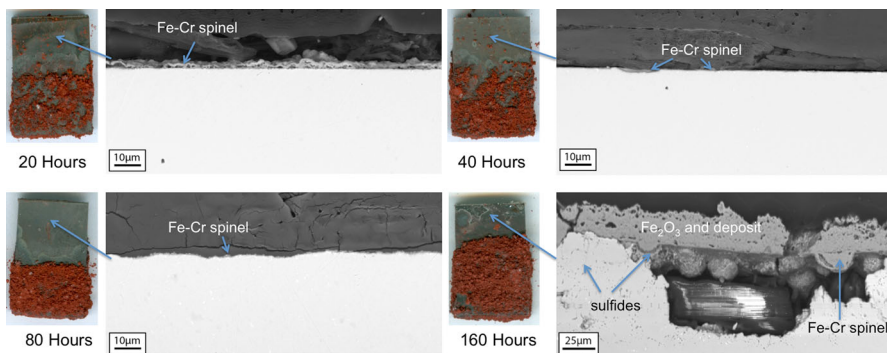


**Fig. 9** Cross-sectional micrographs of the non-deposit zone of T92 tested at 700 °C with the standard corrosion mix powder in a crucible in  $\text{O}_2 + 1000 \text{ ppm SO}_2$  for 20, 40, 80, and 160 h

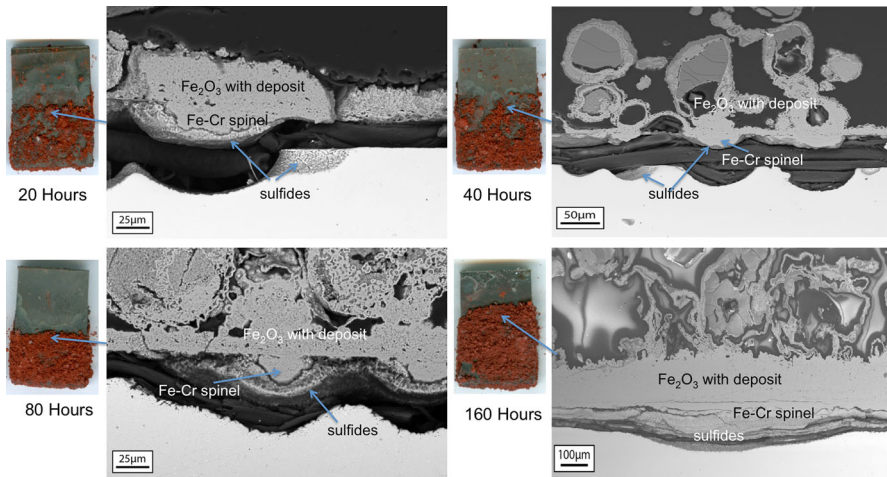


**Fig. 10** Cross-sectional micrographs of the thin deposit zone of T92 tested at 700 °C with the standard corrosion mix powder in a crucible in  $O_2 + 1000 \text{ ppm SO}_2$  for 20, 40, 80, and 160 h

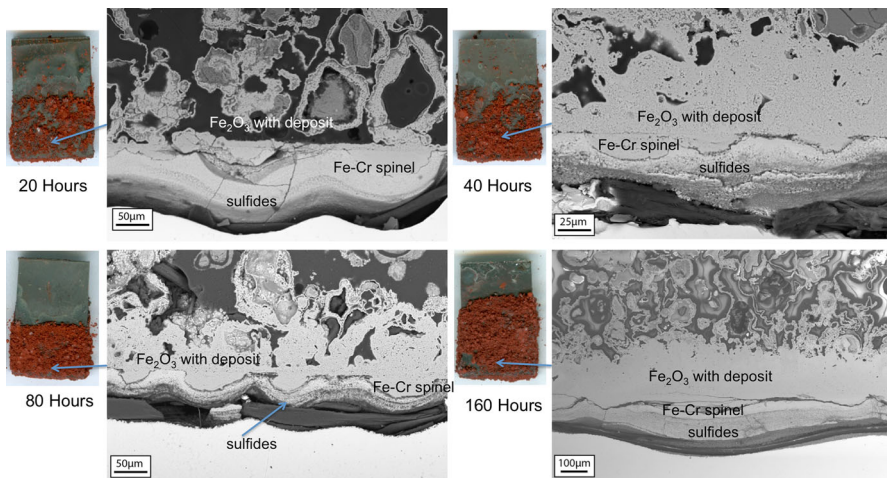


**Fig. 11** Cross-sectional micrographs of the thick deposit zone of T92 tested at 700 °C with the standard corrosion mix powder in a crucible in  $O_2 + 1000 \text{ ppm SO}_2$  for 20, 40, 80, and 160 h

Cross-sectional SEM images for each deposit zone for FeNiCr at each of the test durations are shown in Figs. 12, 13 and 14. In the no-deposit zone, thin iron and chromium rich spinel oxides grew on the surface. After 160 h a thicker scale formed with some internal sulfides. The amount of corrosion in the deposit zones matches well with the metal loss plots. After 20 and 40 h, there was minimal corrosion of the specimens. Thin iron and chromium rich oxides were present throughout the deposit zone. A thicker  $Fe_2O_3$  scale grew around the hole in the specimen in some of the tests, but this can be explained by edge effects. After 80 h there were some small

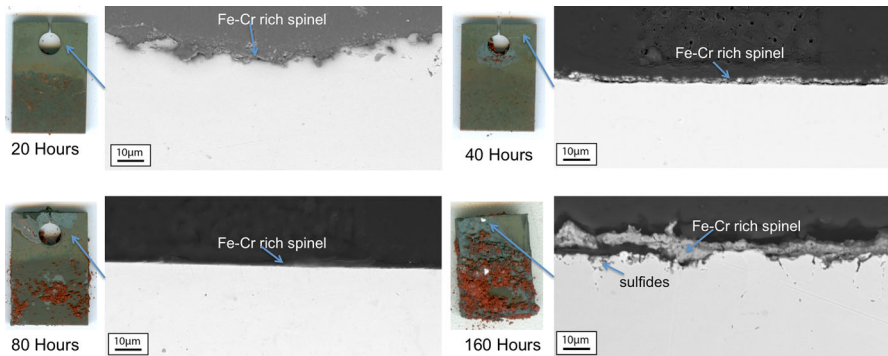


**Fig. 12** Cross-sectional micrographs of the non-deposit zone of FeNiCr tested at 700 °C with the standard corrosion mix powder in a crucible in  $O_2 + 1000$  ppm  $SO_2$  for 20, 40, 80, and 160 h

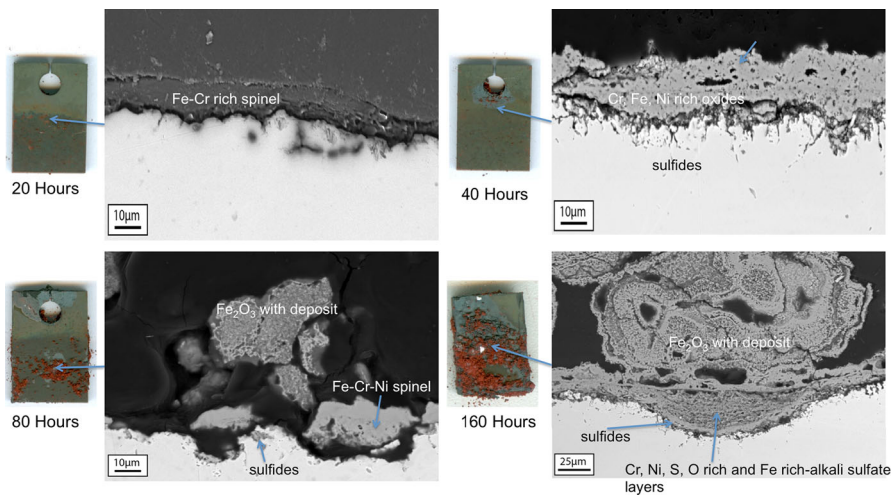


**Fig. 13** Cross-sectional micrographs of thin deposit zone of FeNiCr tested at 700 °C with the standard corrosion mix powder in a crucible in  $O_2 + 1000$  ppm  $SO_2$  for 20, 40, 80, and 160 h

areas of severe degradation in the thin deposit zone. As was mentioned previously, the propagation of corrosion accelerated sometime after 80 h for this alloy. It is at this point in which thick external  $Fe_2O_3$  grew on the surface and corrosion pits began to form. The degradation occurred first in areas where the deposit was the thinnest. The thicker deposit zones likely prevent the  $SO_3$  gas from reaching the surface of the metal as quickly as in the thin deposit zones. The entire deposit region was degraded after 160 h. The corrosion products consisted of thick external porous  $Fe_2O_3$  with adherent deposit materials over more Cr, Fe, and Ni oxide rich pits. The pits had the repeating layers rich in Cr, S, O and Fe, Na, K, S, O seen previously with the M1 deposit. The amount of sulfur increased with depth into the pit until at the base there was a layer rich in Cr and S.

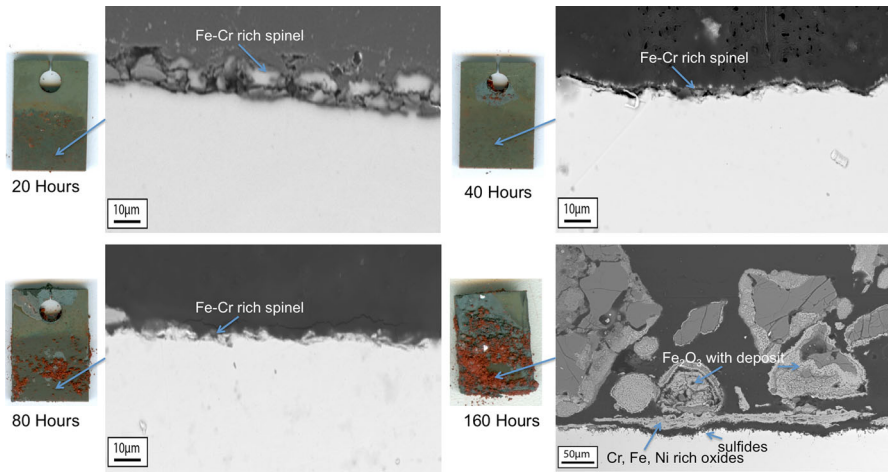


**Fig. 14** Cross-sectional micrographs of the thick deposit zone of FeNiCr tested at 700 °C with the standard corrosion mix powder in a crucible in O<sub>2</sub> + 1000 ppm SO<sub>2</sub> for 20, 40, 80, and 160 h

### Discussion

Metal loss plots comparing the M1 and SCM deposits (thick deposit measurements) are shown in Fig. 15. It was originally thought that the SCM would be the most corrosive deposit used because alkali iron trisulfates could form in the deposit and did not need a thermally grown iron oxide scale. Alkali iron trisulfates form by reaction of iron oxide (either in the deposit or from a thermally grown oxide scale) with alkali sulfates in the deposit and SO<sub>3</sub> in the gas atmosphere. The formation of liquid alkali iron trisulfates at the expense of a thermally grown iron oxide scale was originally thought to be important in the amount of degradation which occurs. It was originally thought that the rapid removal of Fe from the alloy could disrupt protective Cr<sub>2</sub>O<sub>3</sub> scale formation and the mechanism for the disruption of a protective scale may be the similar to Type II hot corrosion described by Luthra

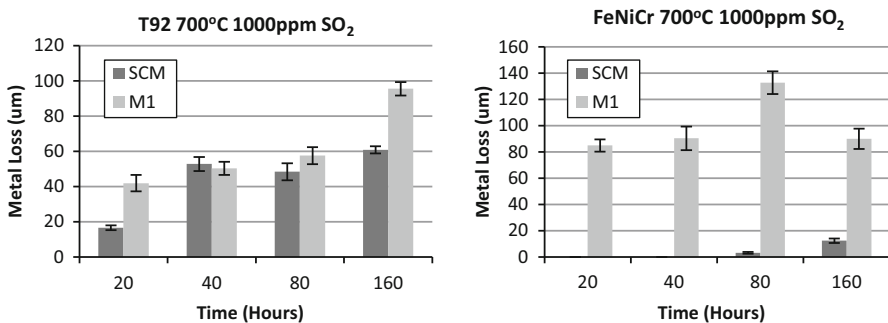


**Fig. 15** Comparison of thick deposit zone metal loss for T92 and FeNiCr exposed in the M1 and SCM deposits at 700 °C in O<sub>2</sub> + 1000 ppm SO<sub>2</sub> for 160 h

[14]. However, the fact that the M1 deposit was more corrosive than the SCM indicates that alkali iron trisulfates may not be the primary cause of severe corrosion and that reactions with alkali sulfates are causing severe degradation, and the process would therefore be similar to Type II hot corrosion caused by  $\text{Na}_2\text{SO}_4$  salt deposits. Type II hot corrosion in gas turbine engines typically occurs at temperatures around  $700\text{ }^\circ\text{C}$  (same temperature range of interest as fireside corrosion) below the melting point of  $\text{Na}_2\text{SO}_4$  ( $884\text{ }^\circ\text{C}$ ) on Co- and Ni-based superalloys used for engine hardware. When  $\text{SO}_3$  in the gas atmosphere reacts with a thermally grown cobalt or nickel transient oxide scale, it forms a low melting solution ( $(\text{Co,Ni})\text{SO}_4\text{-Na}_2\text{SO}_4$   $T_m = 565\text{ }^\circ\text{C}$ ,  $671\text{ }^\circ\text{C}$  respectively). The  $\text{Fe}_2(\text{SO}_4)_3\text{-K}_2\text{SO}_4$  phase diagram is presented in Fig. 16 [15]. A reliable  $\text{Fe}_2(\text{SO}_4)_3\text{-Na}_2\text{SO}_4$  diagram is not available but one would expect it to behave in a similar way. At  $700\text{ }^\circ\text{C}$  on the diagram, a liquid  $\text{K}_2\text{SO}_4\text{-Fe}_2(\text{SO}_4)_3$  solution will form with small additions of  $\text{Fe}_2(\text{SO}_4)_3$ , and alkali iron trisulfates are not necessary to form liquid at this temperature and therefore are not initially causing corrosion in these atmospheres, which is contradictory to what many believed to be the cause of corrosion for decades. Because the low melting solution forms similarly to Type II hot corrosion and the morphologies are similar, the initiation and propagation stages for fireside corrosion can be modeled after the mechanisms for Type II hot corrosion.

### Proposed Fireside Corrosion Mechanism

Based on the results, the following fireside corrosion initiation and propagation mechanism is proposed. This mechanism involves aspects of the mechanisms of Type II hot corrosion explained by the work of Luthra [14], and the mechanisms of

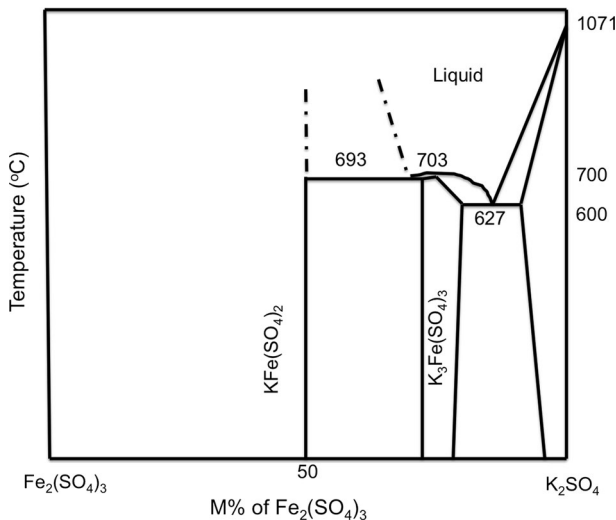


**Fig. 16**  $\text{K}_2\text{SO}_4\text{-Fe}_2(\text{SO}_4)_3$  phase diagram [15]

synergistic dissolution explained by Rapp [16]. During the initiation stage, transient iron oxides and chromium oxide grow on the surface of the alloy. The alloy is covered by the deposit which contains alkali sulfates  $K_2SO_4$  and  $Na_2SO_4$ . The  $SO_3$  from the catalyzed  $O_2 + SO_2$  mixture migrates through the deposit to the oxide/ deposit interface, and when sufficient amounts are present, it reacts with the transient  $Fe_2O_3$  to form  $Fe_2(SO_4)_3$ . When sufficient  $Fe_2(SO_4)_3$  is dissolved in the alkali sulfates the deposit will melt as seen on the phase diagram in Fig. 16. The formation of the liquid salt allows dissolution and fluxing of the protective oxide scales and base metal to take place which is responsible for the lack of protective  $Cr_2O_3$  and the observed metal loss. It is at this point that the propagation stage occurs. The liquid melt forms at the expense of the  $Fe_2O_3$  scale. It was originally thought that formation of the liquid melt from the oxidation of the base metal iron was undercutting and leaving unprotective porous  $Cr_2O_3$  in the melt. The rapid dissolution of the base metal would disrupt protective  $Cr_2O_3$  formation. This is similar to the mechanism proposed by Luthra [14] for Type II hot corrosion. However, the lack of a protective oxide scale and the degradation is more likely due to synergistic dissolution.

The M1 deposit was more corrosive than the SCM. Based on these results, the cause of the increased corrosion of the M1 deposit and the likely controlling fireside corrosion propagation mechanism is synergistic dissolution of oxides in the molten salt deposit similar to that proposed by Rapp for hot corrosion [16]. Once a liquid eutectic melt has formed, it will react with the protective oxide scales and base metal becoming highly basic or acidic and causing dissolution and fluxing, creating the observed corrosion products. The primary elements in the alloy and corrosion

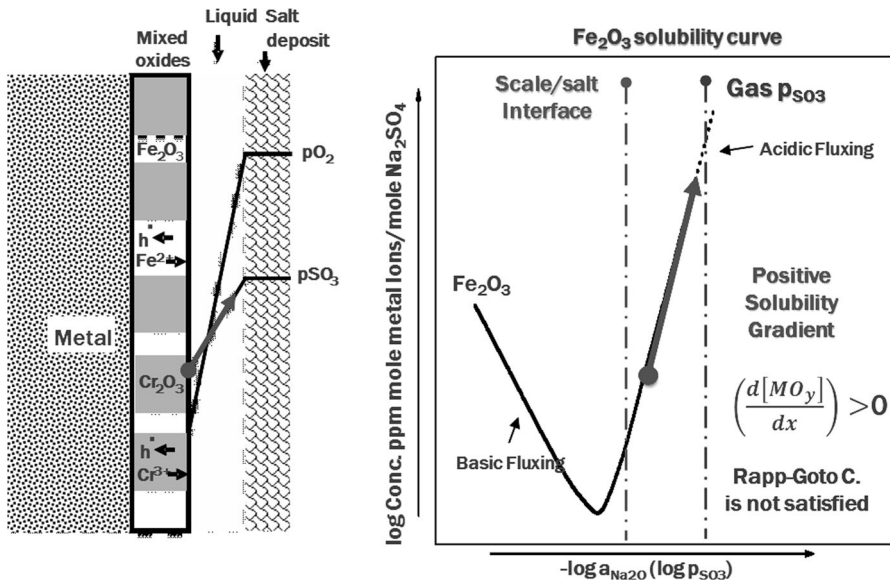
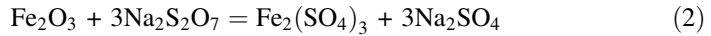


Fig. 17 Schematic of  $SO_3$  gradient at oxide/salt interface and  $Fe_2O_3$  solubility curve for acidic fluxing

products are iron and chromium. They will therefore be the focus of the discussion. The model austenitic alloy contains some Ni and therefore the effect of nickel on the corrosion mechanism will also be briefly discussed. The dissolution reactions for  $\text{Cr}_2\text{O}_3$  and  $\text{Fe}_2\text{O}_3$  are limited by the diffusion of either oxygen or pyrosulfate ( $\text{S}_2\text{O}_7^{2-}$ ) ions. If the oxide dissolution reactions are considered individually,  $\text{Fe}_2\text{O}_3$  would be expected to undergo acidic dissolution in the  $\text{SO}_3$  containing atmosphere with the reaction given in Eq. 2. This reaction would consume  $\text{SO}_3$  in the form of pyrosulfate.



The  $\text{SO}_3$  concentration would be greater at the gas/salt interface than at the oxide/salt interface, setting up a positive solubility gradient at the oxide/salt interface. This is demonstrated by the schematic diagram and solubility plot for  $\text{Fe}_2\text{O}_3$  in  $\text{Na}_2\text{SO}_4$  in Fig. 17. The Rapp–Goto criterion [17] states that a negative solubility gradient is needed for the dissolution of the oxide scale at the oxide/salt interface and precipitation as non-protective discontinuous particles at a distance further out in the melt where the solubility is lower. Acidic dissolution of  $\text{Fe}_2\text{O}_3$  would produce a positive solubility gradient, so the oxide would become saturated in the melt near the oxide/salt interface, minimizing further dissolution.

Luthra states that, in an acidic  $\text{SO}_3$  gas atmosphere,  $\text{Cr}_2\text{O}_3$  would dissolve primarily as its sulfate so basic dissolution should not occur [14]. The  $\text{SO}_3$  concentration would have to be quite high for this to be the case, which suggests that  $\text{Cr}_2\text{O}_3$  could undergo basic dissolution in this atmosphere.  $\text{Cr}_2\text{O}_3$  could also undergo acidic dissolution, given by the reaction in Eq. 3, however a positive solubility

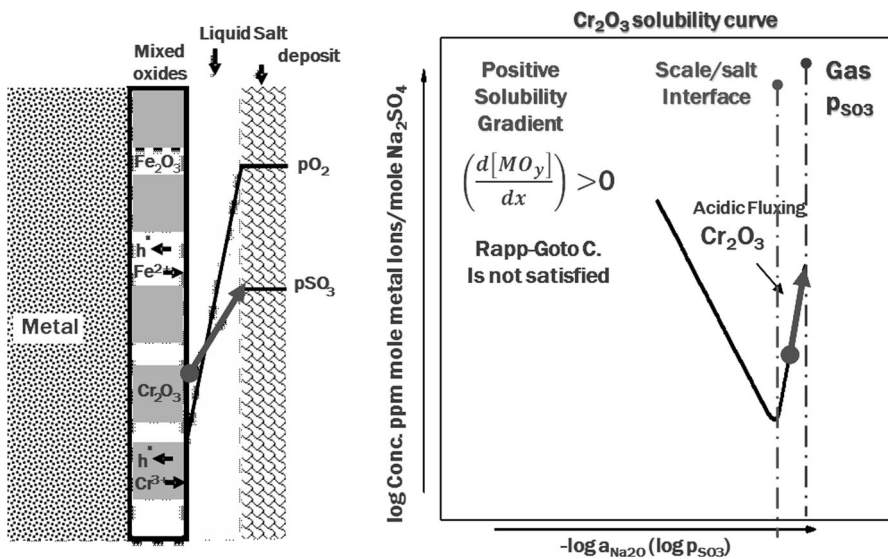
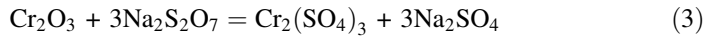


**Fig. 18** Schematic of  $\text{SO}_3$  gradient at oxide/salt interface and  $\text{Cr}_2\text{O}_3$  solubility curve for acidic fluxing



gradient would also be set up at the oxide/salt interface and the protective scale would remain intact. This is demonstrated in Fig. 18.



When the two oxides are both in contact with the salt deposit and the melt basicity is in a position between the solubility minima for  $\text{Fe}_2\text{O}_3$  and  $\text{Cr}_2\text{O}_3$ , then rapid degradation can occur when one oxide undergoes basic dissolution and the other undergoes acidic dissolution. Synergistic fluxing and the simultaneous occurrence of the two dissolution reactions for  $\text{Cr}_2\text{O}_3$  and  $\text{Fe}_2\text{O}_3$  could support each other by creating negative solubility gradients for both species and accelerating corrosion by short circuiting the rate-limiting diffusion process [16]. Initially,  $\text{Fe}_2\text{O}_3$  would be used to help form the liquid  $(\text{Na,K})_2\text{SO}_4\text{-Fe}_2\text{SO}_4$  solution, and locally  $\text{Fe}_2\text{O}_3$  would experience acidic dissolution described by Eq. 4, consuming  $\text{SO}_3$ . The oxide ions released upon acidic dissolution of  $\text{Fe}_2\text{O}_3$  in turn supply the reactant anions needed for basic dissolution of  $\text{Cr}_2\text{O}_3$  [16]. The protective  $\text{Cr}_2\text{O}_3$  scale initially grown by the alloy would experience basic dissolution described by Eq. 5, locally creating  $\text{SO}_3$  (in the form of pyrosulfate) and consuming oxygen. The basic dissolution of  $\text{Cr}_2\text{O}_3$  disrupts protective scale formation.

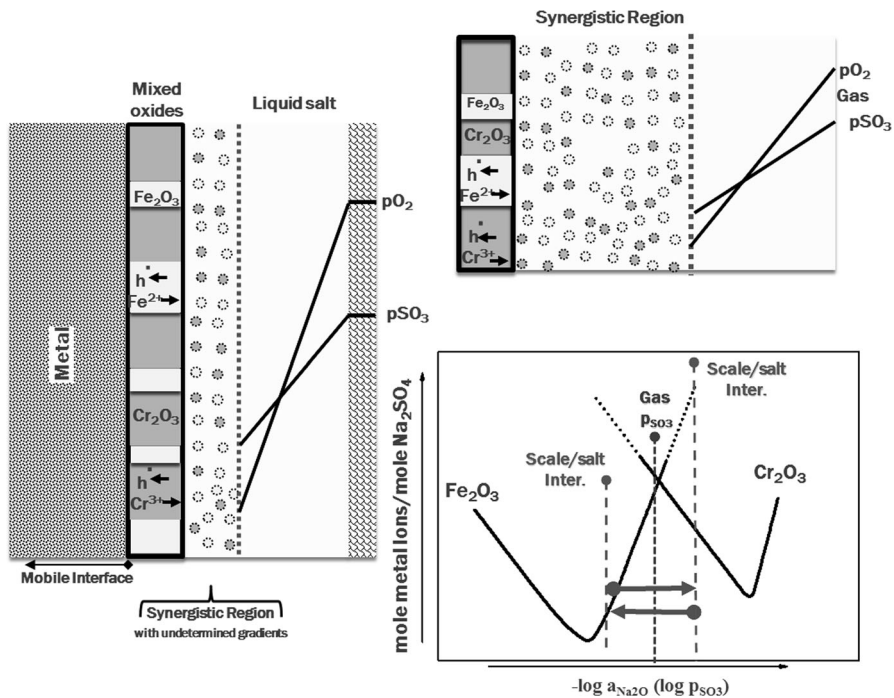
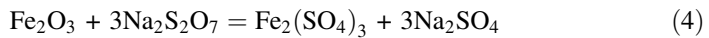
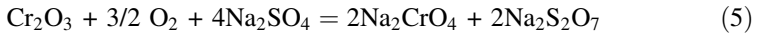


**Fig. 19** Schematic and solubility curves demonstrating synergistic fluxing the repeating acidic and basic dissolution reactions



The basic dissolution of the  $\text{Cr}_2\text{O}_3$  and the local formation of  $\text{SO}_3$  makes the melt more acidic so that the melt is then under favorable conditions for acidic dissolution of the  $\text{Fe}_2\text{O}_3$ . This can repeat indefinitely, so that repeating acidity and basicity of the melt would produce a continuous cycle of accelerated corrosion. The layered corrosion products mentioned in the previous sections supports this repeating cycle. The repeating of the basic and acidic dissolution reactions is shown in the schematic diagrams and solubility curves in Fig. 19. The overall synergistic dissolution reaction is described by Eq. 6. The concentrations of both  $\text{S}_2\text{O}_7^{2-}$  ions and oxygen would be reduced by reaction 6. Therefore, since the dissolution reactions are limited by the diffusion of  $\text{S}_2\text{O}_7^{2-}$  or oxygen, negative solubility gradients at the oxide/salt interface occur during the dissolution process [16]. The arrows in Fig. 19 shows the negative solubility gradients and display the local shift in acidity and basicity of the melt.

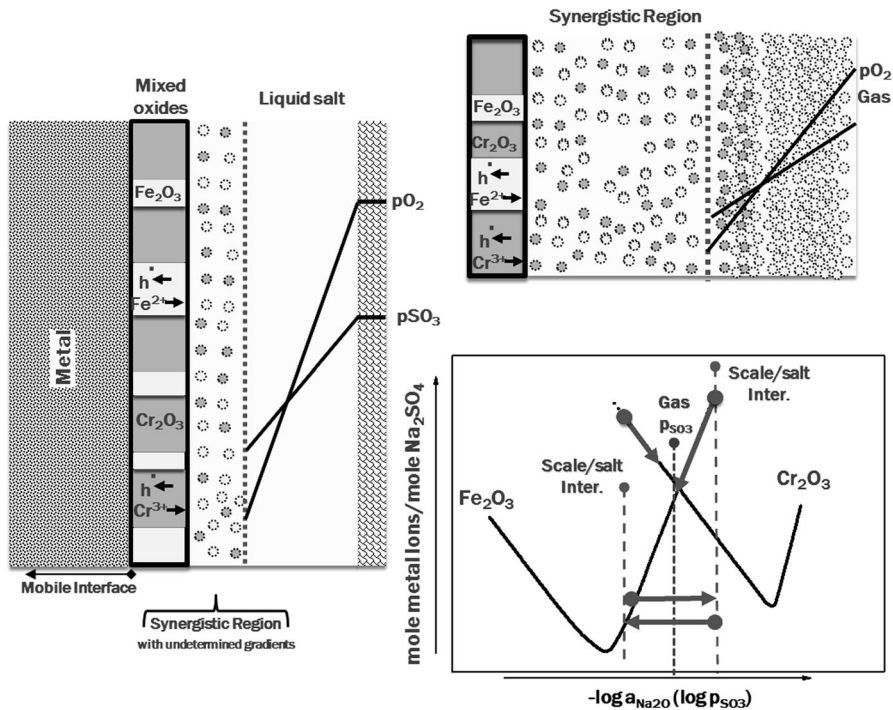
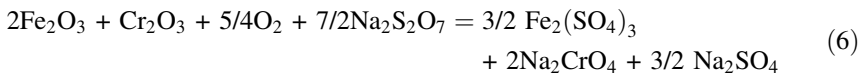


**Fig. 20** Negative solubility gradients on the  $\text{Fe}_2\text{O}_3$  and  $\text{Cr}_2\text{O}_3$  solubility curves due to synergistic fluxing and schematic of precipitation process

The non-protective iron oxide scale observed in the external corrosion products forms when iron oxide is dissolved via Eq. 4 in the synergistic dissolution region at the oxide/salt interface and precipitated in the salt further away from the interface. This is the most significant contribution to the observed metal loss. There is a negative solubility gradient set up where the iron oxide has a higher solubility at the oxide/salt interface than at the gas/salt interface. The iron oxide precipitates where there is a locally low solubility and a higher  $p_{O_2}$ . The chromium solute also experiences a negative solubility gradient. However, the results imply that the solubility of  $Cr_2O_3$  in the melt must be less than that for  $Fe_2O_3$ , because the chromium precipitates earlier, creating the observed internal corrosion pits. The negative solubility gradients and a schematic diagram of the oxide precipitation are presented in Fig. 20. Luthra [14] reported that the solubility of  $Cr_2O_3$  in  $Na_2SO_4$  melts was very low (e.g.  $2 \times 10^{-9}$  at  $p_{SO_3} = 10^{-3}$  atm at 750 °C), so chromium would be expected to stay below the original surface. Nickel oxide was found in small quantities in the internal corrosion pits. The solubility curves for  $NiO$ ,  $Fe_2O_3$ , and  $Cr_2O_3$  in  $Na_2SO_4$  at 927 °C and 1 atm  $O_2$  are presented in Fig. 21. The nickel in the alloy would behave very similarly to the iron in the alloy. It would undergo acidic dissolution similarly in a reaction similar to Eq. 4. The solubility minima for  $NiO$  and  $Cr_2O_3$  are further apart, which may decrease the rate of synergistic dissolution between  $NiO$  and  $Cr_2O_3$ , which may be why it is less prominent in the corrosion products. The solubility of  $NiO$  in the  $(K,Na)_2SO_4$ – $Fe_2(SO_4)_3$  melt is likely also low and therefore is in the internal corrosion pits.

Synergistic fluxing produces negative solubility gradients and the disruption of a protective oxide scale. Once this occurs, degradation continues as the observed porous external iron oxide scale forms over the internal corrosion pits rich in Cr, S,

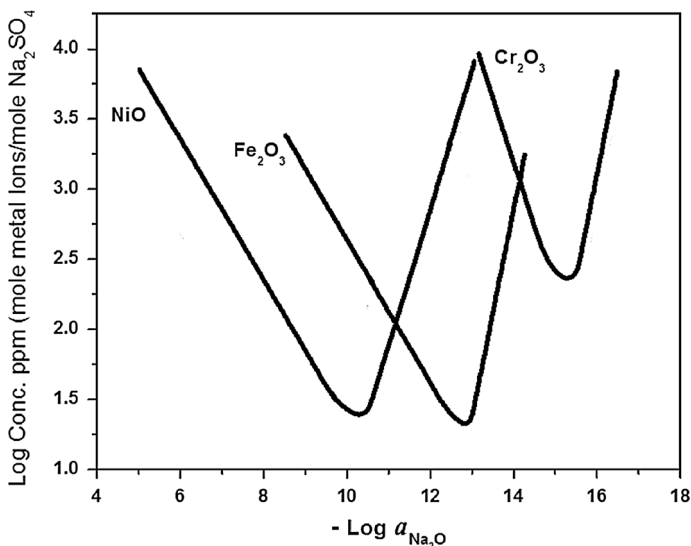


**Fig. 21** Measured oxide solubilities in  $Na_2SO_4$  at 927 °C and 1 atm  $O_2$  [18]

and O. The transport mechanisms of the various species through the liquid melt for the formation of the porous external  $\text{Fe}_2\text{O}_3$  scale and the inward growing corrosion pits can be described similarly to the Type II gas-phase induced acidic fluxing hot corrosion mechanism for Co-based alloys described by Luthra [14]. Inward migrating  $\text{SO}_3$  can pass through the liquid eutectic via an  $\text{S}_2\text{O}_7^{2-}/\text{SO}_4^{2-}$  exchange reaction, where it will react with Cr in the substrate to form the inward growing  $\text{Cr}_2\text{O}_3$  and CrS corrosion pits due to a low  $p_{\text{O}_2}$ , high  $p_{\text{S}_2}/p_{\text{SO}_2}$  at the melt/alloy interface. The external  $\text{Fe}_2\text{O}_3$  scale will simultaneously form via an  $3\text{Fe}^{2+}/2\text{Fe}^{3+}$  exchange reaction similar to that for Co under Type II hot corrosion. The iron reprecipitates as an external porous  $\text{Fe}_2\text{O}_3$  scale at higher  $p_{\text{O}_2}$ .

The proposed fireside corrosion propagation mechanism requires that the salt basicity be between the solubility minima of  $\text{Cr}_2\text{O}_3$  and  $\text{Fe}_2\text{O}_3$ . We can use these curves to determine whether this process is possible under the test conditions. Using the equilibrium  $\text{SO}_3$  partial pressure in  $\text{O}_2 + 1000$  ppm  $\text{SO}_2$ ,  $7.16 \times 10^{-4}$  atm ( $\log p_{\text{SO}_3} = -3.14$ ), then the melt basicity will be between the solubility curves of  $\text{Fe}_2\text{O}_3$  and  $\text{Cr}_2\text{O}_3$  presented in Fig. 21 [16]. The solubility curves constructed by Rapp [18] were at 1200 K however. Leblanc and Rapp [19] studied the solubilities of  $\text{Cr}_2\text{O}_3$  and  $\text{SiO}_2$  in  $\text{Na}_2\text{SO}_4\text{--K}_2\text{SO}_4\text{--Fe}_2(\text{SO}_4)_3$  at 963 K and found that the concentration of soluble  $\text{Cr}_2\text{O}_3$  was six times higher than at 1200 K in  $\text{Na}_2\text{SO}_4$ . This can be seen in Fig. 22. No thermodynamic data is available for the  $(\text{K},\text{Na})_2\text{SO}_4\text{--Fe}_2(\text{SO}_4)_3$  liquid eutectic, but if the equilibrium reaction for sodium sulfate given in Eq. 7 is used along with the equilibrium  $\text{SO}_3$  partial pressure at 700 °C in  $\text{O}_2 + 1000$  ppm  $\text{SO}_2$  of  $7.16 \times 10^{-4}$  atm ( $\log p_{\text{SO}_3} = -3.14$ ), then the equilibrium melt basicity ( $-\log a_{\text{Na}_2\text{O}}$ ) equals 19.23 at 700 °C.

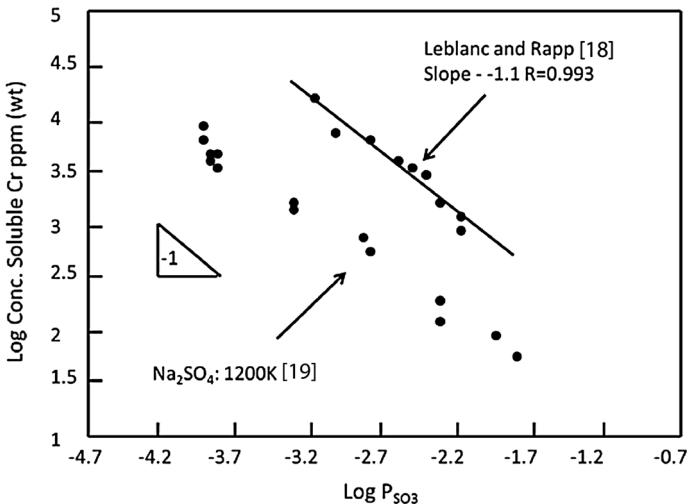


**Fig. 22** Solubility of  $\text{Cr}_2\text{O}_3$  in sulfate melts (top data at 963 K) [19]

With the data from Fig. 22, the  $\text{Cr}_2\text{O}_3$  solubility curve in Fig. 21 would shift to the right and about six times higher in solubility. Assuming at the lower temperature and in the  $\text{Na}_2\text{SO}_4\text{--K}_2\text{SO}_4\text{--Fe}_2(\text{SO}_4)_3$  melt that the  $\text{Fe}_2\text{O}_3$  solubility curve would shift in a similar manner, then synergistic dissolution should be feasible under fireside corrosion conditions. Somewhat complicating such an analysis is that the local basicity can change as the metal or oxide in contact with the sulfate changes as it goes through the synergistic cycles. Otsuka and Rapp [20] simultaneously tracked the basicity and oxygen activity in the substrate-salt interface during hot corrosion of nickel covered by a thin film of  $\text{Na}_2\text{SO}_4$ . Initially the local basicity supported acidic dissolution of a preformed NiO scale (to the right of the NiO solubility minima), but as it was breached, the local basicity changed to support basic dissolution (to the left of the NiO solubility minima). This is a significant observation in that it shows processes occurring at the alloy/salt interface, e.g. dissolution, can be controlled by local conditions rather than the gas phase. Later the local basicity switched back to acidic dissolution.

The addition of either  $\text{Fe}_2\text{O}_3$  to the base M1 deposit (SCM), significantly decreases the amount of metal loss of these alloys. It is proposed the M1 deposit at the salt/gas interface has a melt basicity that is in the solubility range where synergistic dissolution can occur. The SCM is less corrosive than the M1 deposit because the iron oxide in the deposit changes the local basicity of the melt. The melt basicity may no longer be in a region where the maximum corrosion rate can occur. Synergistic dissolution has been slowed down, but not stopped completely. The cycle between acidic and basic fluxing that occurs with synergistic dissolution takes longer due to the change in the basicity with the iron oxide addition. The simultaneous dissolution reactions are no longer able to support each other as quickly.

## Supporting Experiments

To further prove if synergistic dissolution was occurring, the FeNiCr and T92 alloys were exposed to a deposit containing M1 + 30 %  $\text{Cr}_2\text{O}_3$  at 700 °C in  $\text{O}_2$  + 1000 ppm  $\text{SO}_2$  for 160 h. It is thought that synergistic dissolution is occurring with the M1 deposit, and that the addition of  $\text{Fe}_2\text{O}_3$  to the alkali sulfate mix (SCM) is causing the melt to become locally more basic and pushing it out of the solubility region between where synergistic dissolution would occur at a maximum rate. Similarly, the  $\text{Cr}_2\text{O}_3$  in the deposit of M1 + 30 %  $\text{Cr}_2\text{O}_3$  would cause the melt to be locally more acidic and out of the region for synergistic dissolution to occur at a maximum rate. Synergistic dissolution causes the melt to undergo a cycle of basic and acidic fluxing, and changes in the local melt basicity or acidity with the additions of oxides to the alkali sulfates will slow down this cycle and reduce negative the solubility gradients. The results of the test in M1 + 30 %  $\text{Cr}_2\text{O}_3$  are shown in Figs. 23 and 24 as mass change and thick deposit metal loss values compared with the results under the same conditions when using the M1 and SCM deposits. The M1-Cr deposit is even less corrosive than the SCM. The addition of  $\text{Cr}_2\text{O}_3$  increased the local acidity of the melt so much that it essentially

stopped synergistic dissolution from occurring and significantly slowed the corrosion rate. Macroscopic and microscopic cross section images of the results in M1 + 30 % Cr<sub>2</sub>O<sub>3</sub> are shown in Fig. 25. The images presented are the areas of the specimen where the corrosion was the most extensive. There was significantly less degradation when chromia was added to the deposit. T92 had some small areas of localized pitting, and the FeNiCr alloy grew a thick iron and chromium rich oxide scale on the surface with minimal mass change and metal loss.

The effect of other oxide additions commonly found in coal ash to the deposit on the proposed mechanism and the amount of corrosion was also examined. (Al<sub>2</sub>O<sub>3</sub>: M1, SCM-A, CaO: M1, SCM-C, and SiO<sub>2</sub>: M1, SCM-S) Thick deposit metal loss plots are shown in Figs. 26 and 27 compared with the results of the SCM and M1 deposit (The SCM-A and SCM-S bars cannot be seen because the metal loss was minimal).

Alumina in the deposit is reducing the amount of corrosion that occurs. Alumina is a neutral oxide and may undergo acidic or basic fluxing when reacting with alkali sulfates. The SCM already has iron oxide mixed in with the alkali sulfates, which as was shown in the mechanism section, pushes the melt basicity out of the solubility region where synergistic dissolution can occur at a maximum rate. The addition of alumina to the SCM may further shift the melt basicity out of the region where synergistic dissolution can occur at a rapid rate. Because alumina is a neutral oxide and may undergo acidic or basic fluxing when reacting with alkali sulfates, it may react in a basic manner in this case, shifting melt basicity even further away from the maximum synergistic zone. The cycle between acidic and basic fluxing does not occur as rapidly due to the local increase in basicity of the melt. The corrosion mechanism would still be the same as described in the Mechanism Study sections, however the synergistic fluxing rate is slowed down even more compared to the SCM.

The (Na,K)<sub>2</sub>SO<sub>4</sub>–Fe<sub>2</sub>(SO<sub>4</sub>)<sub>3</sub> liquid solution may not be the only liquid that is forming and causing the fluxing that is occurring. The alumina in the deposit may react with alkali sulfates in the deposit and SO<sub>3</sub> in the gas atmosphere to form alkali aluminum trisulfates via the reaction in Eq. 8.

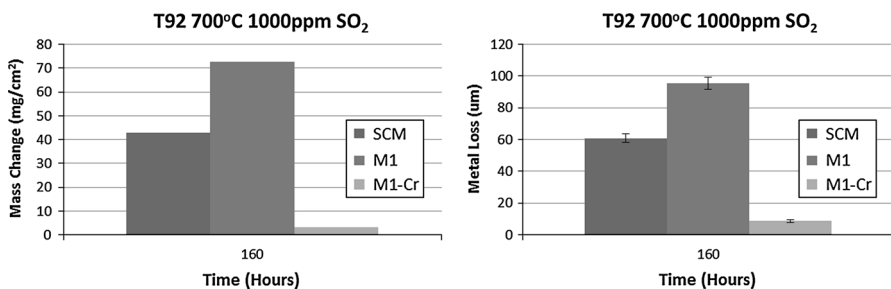
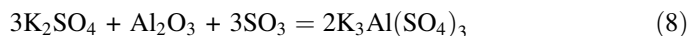


**Fig. 23** Mass change and thick deposit zone metal loss for T92 exposed at 700 °C with the M1, SCM, and M1 + 30 % Cr<sub>2</sub>O<sub>3</sub> powder deposits in a crucible in O<sub>2</sub> + 1000 ppm SO<sub>2</sub> for 160 h

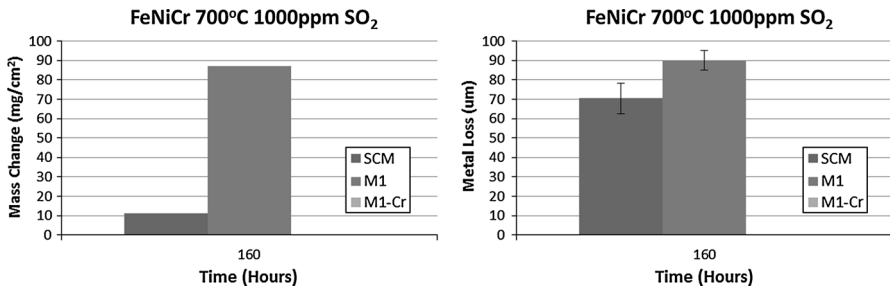


**Fig. 24** Mass change and thick deposit zone metal loss for FeNiCr exposed at 700 °C with the M1, SCM, and M1 + 30 % Cr<sub>2</sub>O<sub>3</sub> powder deposits in a crucible in O<sub>2</sub> + 1000 ppm SO<sub>2</sub> for 160 h

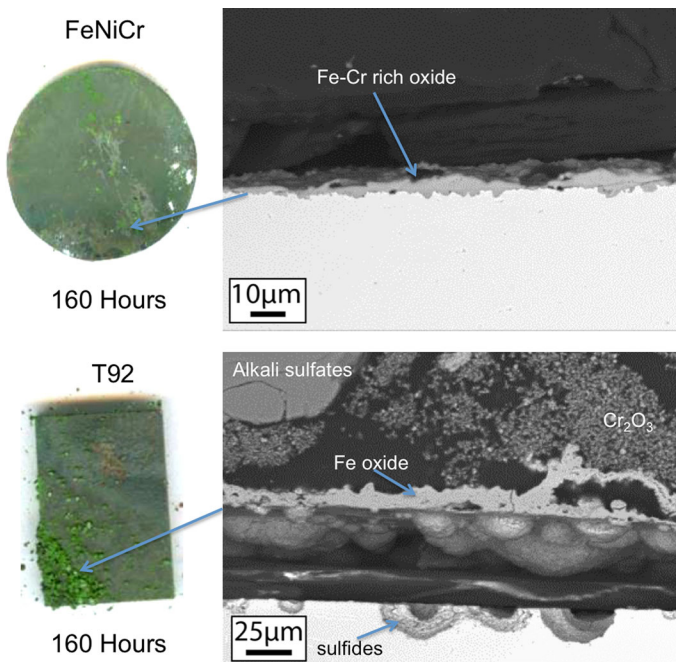


**Fig. 25** Macroscopic and microscopic SEM images of FeNiCr and T92 exposed at 700 °C with M1 + 30 % Cr<sub>2</sub>O<sub>3</sub> powder deposit in O<sub>2</sub> + 1000 ppm SO<sub>2</sub> for 160 h

X-ray diffraction of the corrosion products confirmed that K<sub>3</sub>Al(SO<sub>4</sub>)<sub>3</sub> was present. This can be seen in Fig. 28. Alkali aluminum trisulfate has a melting point of 654 °C, and would be molten at the temperature of interest. The liquid alkali aluminum trisulfates would form in the deposit and not at the expense of a thermally grown iron oxide scale as occurs with the M1 deposit.

Calcia is a highly basic oxide and its addition along with the iron oxide addition to the alkali sulfates in the SCM would make the melt highly basic and therefore much less corrosive. Synergistic fluxing is significantly slowed down due to the

**Fig. 26** Thick deposit zone metal loss of FeNiCr and T92 exposed in various deposits containing the SCM with oxide additions at 700 °C in O<sub>2</sub> + 1000 ppm SO<sub>2</sub> for 160 h

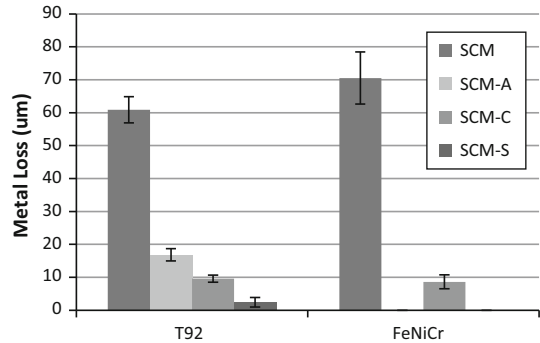
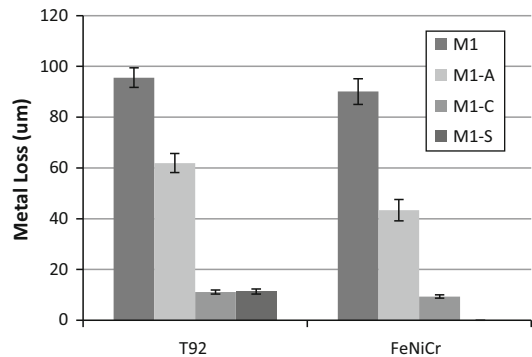
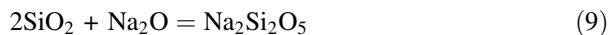


**Fig. 27** Thick deposit zone metal loss of FeNiCr and T92 exposed in various deposits containing M1 with oxide additions at 700 °C in O<sub>2</sub> + 1000 ppm SO<sub>2</sub> for 160 h



localized increase in basicity of the melt. Calcia is more basic than alumina, so the effects are even greater. The SCM-C deposit is also likely less corrosive than the SCM and even the SCM-A deposit, because calcia can react with SO<sub>3</sub> in the gas to form CaSO<sub>4</sub>, and this can further react with alkali sulfates in the deposit to form K<sub>2</sub>Ca<sub>2</sub>(SO<sub>4</sub>)<sub>3</sub>, which has a melting point of 875 °C. It will not be liquid at the temperature range of interest and therefore not corrosive. The CaSO<sub>4</sub> ties up alkali sulfates making less available to form the (Na,K)<sub>2</sub>SO<sub>4</sub>-Fe<sub>2</sub>(SO<sub>4</sub>)<sub>3</sub> liquid and causing corrosion [4]. It also locally ties up SO<sub>3</sub> and possibly increases the local basicity of the melt. X-ray diffraction scans of the powder corrosion products were able to identify CaSO<sub>4</sub> and K<sub>2</sub>Ca<sub>2</sub>(SO<sub>4</sub>)<sub>3</sub>. This is shown in Fig. 29.

Silica is a highly acidic oxide that undergoes basic dissolution when reacting with alkali sulfates. The dissolution of silica in liquid sodium sulfate melts can be described by the reaction in Eq. 9.



Jacobson [21] calculated the minimum Na<sub>2</sub>O activity and maximum p<sub>SO<sub>3</sub></sub> to form Na<sub>2</sub>Si<sub>2</sub>O<sub>5</sub> and cause dissolution of SiO<sub>2</sub> from 900 to 1200 °C. This is shown in Table 4. The minimum Na<sub>2</sub>O activity and the maximum p<sub>SO<sub>3</sub></sub> decreases as the temperature decreases. There is no data for 700 °C, but if this trend is continued, the



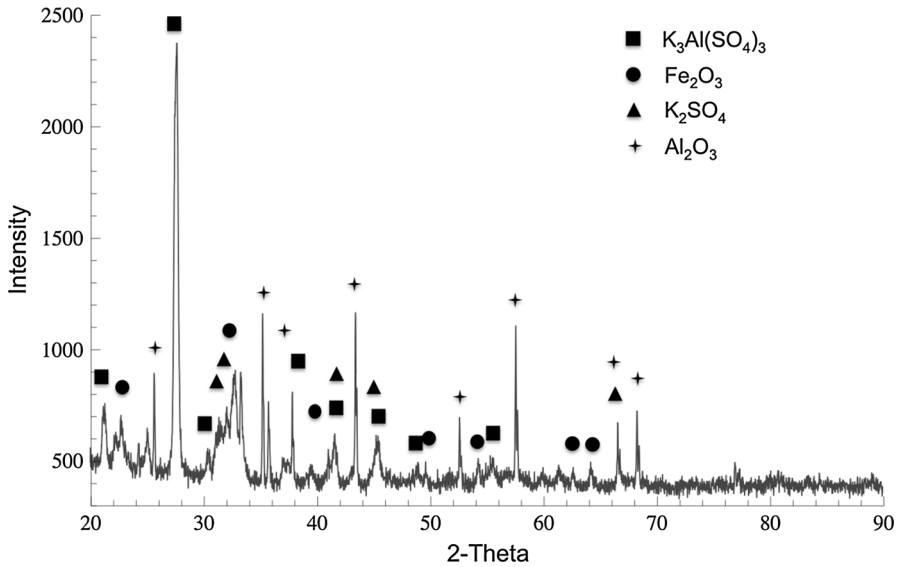


**Fig. 28** X-ray diffraction scan of powder corrosion products of SCM-A after exposure in  $O_2 + 1000 \text{ ppm } SO_2$

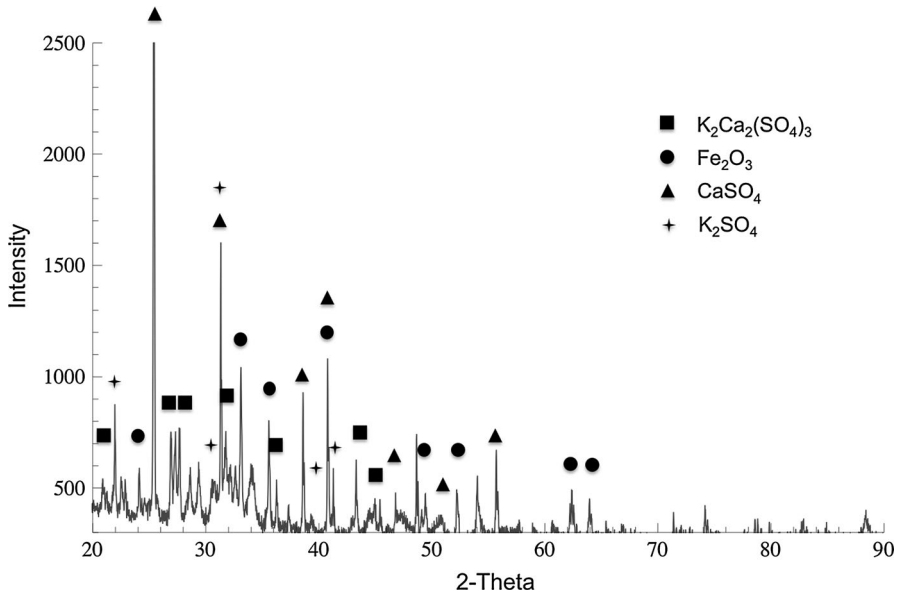


**Fig. 29** X-ray diffraction scan of powder corrosion products of SCM-C after exposure in  $O_2 + 1000 \text{ ppm } SO_2$

relatively high  $\text{SO}_3$  partial pressures of  $1.76 \times 10^{-4}$  atm used in this study and low calculated  $\text{Na}_2\text{O}$  activity at 700 °C of  $1.82 \times 10^{-20}$  may actually prevent the dissolution of silica. The formed  $\text{Na}_2\text{Si}_2\text{O}_5$  has a melting point of 874 °C, and would remain solid and be non-reactive at the temperature of interest for this study. The data by Jacobson was for temperatures above the melting point of  $\text{Na}_2\text{SO}_4$  (884 °C) and  $\text{Na}_2\text{Si}_2\text{O}_5$  and may not be accurate in describing the dissolution at 700 °C in ternary melts. Leblanc and Rapp [19] measured the solubility of  $\text{SiO}_2$  in  $\text{Na}_2\text{SO}_4$ – $\text{K}_2\text{SO}_4$ – $\text{Fe}_2\text{SO}_4$  melts at 963 K (690 °C). They observed that there was no apparent dependence of the measured solubilities on  $p_{\text{SO}_3}$ , which indicated that the dissolution of  $\text{SiO}_2$  in ternary melts at temperatures around 700 °C takes place by molecular dissolution without a chemical reaction. The solubility was also about three times higher than that found by Rapp in Fig. 21. This can be seen in Fig. 30. The solubility measurements compared were obtained by two different techniques (atomic absorption and colorimetric absorption). An increase in the solubility of molecular species in aqueous solution with decreasing temperature is observed, therefore, silica dissolving as a molecular species in the salt could behave in the same way [20]. Silica may be reacting to form the higher melting  $\text{Na}_2\text{Si}_2\text{O}_5$ . The formation of higher melting compounds is reducing the amount of alkali sulfates available to form the liquid solution and allow corrosion to occur. X-ray diffraction scans of the exposed deposit corrosion products were unable to specifically identify  $\text{Na}_2\text{Si}_2\text{O}_5$ , however unidentified peaks are likely a complex compound containing Si, Na, K, S, and/or O. This may be an amorphous structure and unidentifiable with X-ray diffraction. Previous studies by Niles and Sigmund [22] tested kaolin ( $\text{Al}_2\text{O}_3 \cdot 2\text{SiO}_2$ ) as an additive to deposits and they found that it is effective in reacting with sodium sulfate. They described it as the alumina and silica inhibiting the corrosion by absorbing the corrosive molten sulfates. The results of the tests from this study support this.

Finally, although the experiments described in this paper were all conducted using  $\text{O}_2 + 1000$  ppm  $\text{SO}_2$ , additional experiments were conducted using both higher and lower  $\text{SO}_2$  contents with the result that the corrosion rate increased as the  $\text{SO}_3$  partial pressure increased. These observations are consistent with the proposed mechanism in that a higher  $\text{SO}_3$  partial pressure will:

- Accelerate the melting of the salt and produce a larger amount of liquid.
- Accelerate the basic fluxing of the chromia by shortening the distance at which reprecipitation will occur.

**Table 4** Minimum  $\text{Na}_2\text{O}$  activities and maximum  $p_{\text{SO}_3}$  partial pressures for  $\text{SiO}_2$  dissolution [20]

T (°C)	a ( $\text{Na}_2\text{O}$ )	$p_{\text{SO}_3}$	$p_{\text{SO}_2}$
900	$2.0 \times 10^{-11}$	$3.4 \times 10^{-7}$	$1.0 \times 10^{-6}$
1000	$9.2 \times 10^{-11}$	$4.9 \times 10^{-6}$	$3.2 \times 10^{-5}$
1100	$3.6 \times 10^{-10}$	$4.9 \times 10^{-5}$	$6.1 \times 10^{-4}$
1200	$1.4 \times 10^{-9}$	$3.6 \times 10^{-4}$	$7.8 \times 10^{-3}$

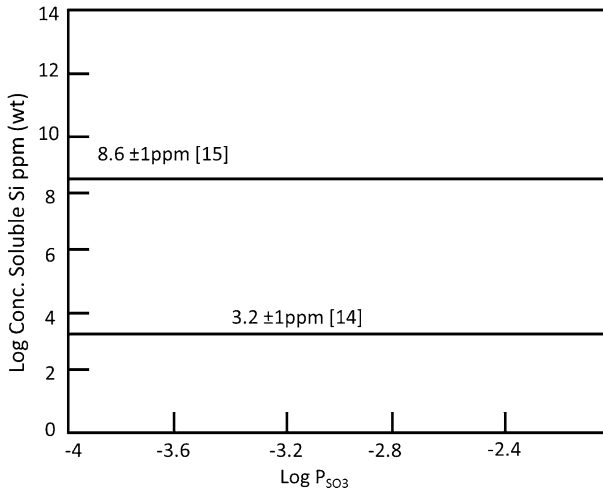


**Fig. 30** Solubility of  $\text{SiO}_2$  in sulfate melts [19]

## Conclusions

The fireside corrosion resistance of two chromia-forming alloys was studied in simplified combustion atmospheres with synthetic deposits to examine potential rate controlling propagation mechanisms and compositional effects. Fireside corrosion has been believed for many years to result from the formation of liquid alkali iron trisulfates on the surface of superheater tubes. The results of the experiments indicated the following:

- The corrosion products for both of the alloys were similar. Thick porous external iron oxide scales grew over internal corrosion pits rich in Cr, S, and O, with a sulfide rich layer at the base of the pits.
- The FeNiCr alloy exhibited two-stage kinetics when using the SCM: an initiation stage during which degradation is slow followed by a propagation stage during which degradation is rapid. The T92 alloy did not exhibit an initiation stage. This is most likely due to the lower Cr content in T92.
- Corrosion appears to initiate in the thin deposit region, with the formation of a liquid salt preceding severe degradation.
- Weight changes and the amount of degradation are more severe with M1 than with the SCM.
- A synergistic dissolution corrosion mechanism was proposed based on the analysis of the results in this study. The liquid salt that is forming is a  $(\text{Na},\text{K})_2\text{SO}_4\text{-Fe}_2(\text{SO}_4)_3$  solution similar to those formed in Type II hot corrosion of Ni and Co-based alloys. Alkali iron trisulfates are not needed to form the liquid deposit, and are not likely the corrosive species causing degradation.

- Synergistic dissolution creates negative solubility gradients for  $\text{Fe}_2\text{O}_3$  and  $\text{Cr}_2\text{O}_3$  and accelerates corrosion by “short circuiting” the rate limiting diffusion process of  $\text{SO}_3$  migrating through the melt.
  - Synergistic dissolution disrupts protective oxide formation. The oxides precipitate where there is lower solubility, creating the observed corrosion products.
  - Inward migrating  $\text{SO}_3$  can pass through the liquid salt via an  $\text{S}_2\text{O}_7^{2-}/\text{SO}_4^{2-}$  exchange reaction, where it will react with Cr in the substrate to form the inward growing  $\text{Cr}_2\text{O}_3$  and CrS corrosion pits due to a low  $p_{\text{O}_2}$ , and high  $p_{\text{S}_2}/p_{\text{SO}_2}$  at the melt/alloy interface.
  - The external  $\text{Fe}_2\text{O}_3$  scale will simultaneously form via an  $3\text{Fe}^{2+}/2\text{Fe}^{3+}$  exchange reaction similar to that for Co under Type II hot corrosion. The iron precipitates as an external porous  $\text{Fe}_2\text{O}_3$  scale at higher  $p_{\text{O}_2}$ .
- Oxides added to the alkali sulfates change the local melt basicity so that synergistic fluxing is no longer able to occur at a rapid rate.

**Acknowledgments** This work at University of Pittsburgh was performed in support of the National Energy Technology Laboratory’s ongoing research on Advanced Combustion under RUA Contract URS-168.

**Disclaimer** This report was prepared as an account of work sponsored by an agency of the United States Government. Neither the United States Government nor any agency thereof, nor any of their employees, makes any warranty, express or implied, or assumes any legal liability or responsibility for the accuracy, completeness, or usefulness of any information, apparatus, product, or process disclosed, or represents that its use would not infringe privately owned rights. Reference herein to any specific commercial product, process, or service by trade name, trademark, manufacturer, or otherwise does not necessarily constitute or imply its endorsement, recommendation, or favoring by the United States Government or any agency thereof. The views and opinions of authors expressed herein do not necessarily state or reflect those of the United States Government or any agency thereof.

### Compliance with Ethical Standards

**Conflict of interest** The authors declare they have no conflict of interest.

**Research involving human participants and/or animals and informed consent** There were no human participants or animals in this study.

## References

1. J. Stringer and I. G. Wright, *Oxidation of Metals* **44**, 265–308 (1995).
2. A. U. Syed, N. J. Simms and J. E. Oakey, *Fuel* **101**, 62–73 (2012).
3. G. P. Huffman and F. E. Huggins, *Reactions and Transformations of Coal Mineral Matter at Elevated Temperatures*. U.S. Steel Corporation Technical Center, Monroeville, PA. The American Chemical Society, Vol. 188. No. 1155, 1984.
4. W. T. Reid, *External Corrosion and Deposits Boilers and Gas Turbines*, (American Elsevier Publishing Company Inc., New York, 1971).

5. M. S. Gagliano, H. Hack and G. Stanko, *Fireside Corrosion Resistance of Proposed USC Superheater and Reheater Materials: Laboratory and Field Test Results*. Presented at the 33th International Technical Conference on Coal Utilization and Fuel Systems, 2008.
6. K. Natesan, A. Purohit and D. L. Rink, *Fireside Corrosion of Alloys for Combustion Plants*. Proceedings 16th Annual Conference on Fossil Energy Materials, Baltimore, MD, April 22–24, 2002.
7. H. Hack and G. Stanko, *Experimental Results for Fireside Corrosion Resistance of Advanced Materials in Ultra-Supercritical Coal-Fired Power Plants*. Presented at the 32nd International Technical Conference on Coal Utilization & Fuel Systems, 2007.
8. G. H. Meier, K. Jung, N. Mu, N. M. Yanar, F. S. Pettit, J. P. Abellán, T. Olszewski, L. N. Hierro, W. J. Quadackers and G. R. Holcomb, *Oxidation of Metals* **74**, 319–340 (2010).
9. T. Hussain, A. U. Syed and N. J. Simms, *Fuel* **113**, 787–797 (2013).
10. Corrosion of metals and alloys-methods for metallographic examination of samples after exposure to high temperature corrosive environments. In: Draft ISO Standard. ISO/TC 156 NWI 5092005; 2006.
11. B. Pujilaksono, T. Jonsson, H. Heidari, M. Halvarsson, J. E. Svensson and L. G. Johansson, *Oxidation of Metals* **75**, 183–207 (2011).
12. T. Jonsson, J. Froitzheim, J. Pettersson, J.-E. Svensson, L.-G. Johansson and M. Halvarsson, *Oxidation of Metals* **72**, 213–239 (2009).
13. J. Topfer, S. Aggarwal and R. Dieckmann, *Solid State Ionics* **81**, 251–266 (1995).
14. K. L. Luthra, *Metallurgical Transactions A* **13**, 1853–1864 (1982).
15. A. Rahmel and W. Jaeger, *Zeitschrift für anorganische und allgemeine Chemie* **330**, 90–95 (1960).
16. Y. S. Hwang and R. A. Rapp, *Journal of the Electrochemical Society* **137**, 1276–1280 (1990).
17. R. A. Rapp and K. S. Goto, *The Hot Corrosion of Metals by Molten Salts*. The Second International Symposium on Molten Salts, (Electrochem. Soc., Pennington, NJ, 1981), pp. 159–171.
18. R. A. Rapp, *Corrosion* **42**, 568–577 (1986).
19. P. P. Leblanc and R. A. Rapp, *Journal of the Electrochemical Society* **140**, L41–L43 (1993).
20. N. Otsuka and R. A. Rapp, *Journal of the Electrochemical Society* **137**, 46–52 (1990).
21. N. S. Jacobson, *Oxidation of Metals* **31**, 91–103 (1989).
22. W. D. Niles and C. W. Siegmund, *The Mechanism of Corrosion by Fuel Impurities*, (Butterworths, London, 1963), pp. 332–334.